J Adv Ceram

Research Article

Abnormal dielectric behavior of glaserite-type $Ba_{3-x}Sr_xMgSi_2O_8$ solid solution

Jiaqing Yang[1,2], Peng Lei[1], Xiaoqiang Song[2], Changzhi Yin[2], Meng Zhang[1,2], Weicheng Lei[1,2], Yiyang Cai[1,2], Mingfei Cheng[1,2], Yaodong Liu[1,2], Zihang Chen[1,2], Yaqing Hu[1,2], Wenzhong Lu[1,2], Wen Lei[1,2]✉

Cite this article: Yang J, Lei P, Song X, et al. *J Adv Ceram* 2025, **14**(2): 9221020. https://doi.org/10.26599/JAC.2024.9221020

ABSTRACT: The temperature coefficient of the resonant frequency (τ_f) of low-permittivity (ε_r) microwave dielectric ceramics is required to be near 0 ppm/°C for practical application. However, owing to the polarization mechanism, τ_f of low-ε_r microwave dielectric ceramics is generally negative. Here, a novel microwave dielectric ceramic, $Ba_{3-x}Sr_xMgSi_2O_8$, with an abnormal positive τ_f at the applied temperature is presented. In this study, Sr^{2+} with a relatively small ionic radius was introduced to replace Ba^{2+}, and a single-phase solid solution was formed ($x > 0.5$). $Ba_{3-x}Sr_xMgSi_2O_8$ ceramics were discussed in glaserite-type topology with space groups of $P\bar{3}$ for $x \le 0.5$, relatively high symmetry $P\bar{3}m1$ for $0.5 < x < 2.5$, and $C2$ for $x \ge 2.5$. The ε_r peaks as a function of temperature initially shift to low temperatures and then return to high temperatures through an ion substitution strategy. Notably, remarkable microwave dielectric properties for $BaSr_2MgSi_2O_8$ were observed: $\varepsilon_r \approx 14.2$, $Q\times f \approx 38{,}900$ GHz, and $\tau_f \approx +117$ ppm/°C, which are superior to those of other low-ε_r silicate ceramics with positive τ_f values. Density functional theory simulation calculations revealed that the preferential occupation of Sr^{2+} ions could decrease the intrinsic formation energy and improve the microwave dielectric properties by mitigating the ionic size mismatch within the crystal structure. The present research offers a strategy for discovering novel microwave dielectric ceramics with abnormal τ_f values, which could serve as τ_f regulators in practical applications because of their low cost and excellent microwave dielectric properties.

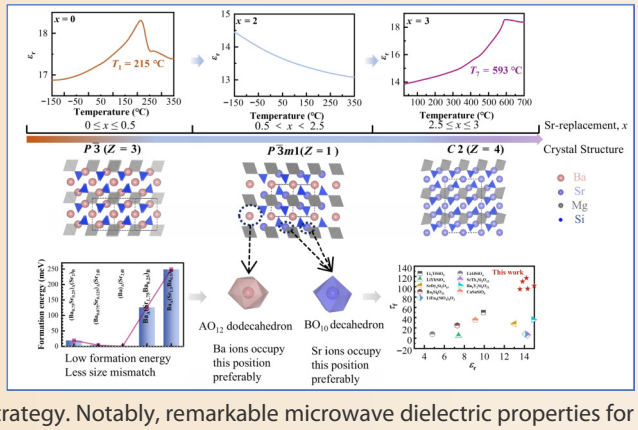

KEYWORDS: microwave dielectric ceramics; abnormal dielectric behavior; ion size mismatch; [SiO_4] tetrahedra tilting; phase transition; density functional theory (DFT)

1 Introduction

The advancement of microwave circuits necessitates the development of more sophisticated passive components, among which the performance of dielectric materials plays a crucial role [1]. In millimeter-wave communication, microwave dielectric ceramics with low-permittivity ($\varepsilon_r \le 15$), high $Q\times f$, and near zero resonant frequency ($-10 \le \tau_f \le +10$ ppm/°C) are needed. However, τ_f for low-ε_r microwave ceramic materials is generally negative, which is determined by their polarization mechanism within the microwave frequency range [1,2]. Therefore, ceramics with opposite τ_f values are often used for adjustment by forming composites or solid solutions, such as TiO_2, $CaTiO_3$, and $SrTiO_3$, which have large positive τ_f values [3–6]. However, these composites significantly increase ε_r, exhibit nonlinear effects, and pose challenges for co-firing with base metal electrodes owing to the variable chemical valence of Ti [7–9]. Consequently, there is an urgent need to develop new low-ε_r microwave dielectric ceramics with abnormally positive τ_f values, as exemplified by several representative systems outlined in Table 1.

For example, $A_3(VO_4)_2$ (A = Ba, Sr) systems can effectively improve τ_f of various systems, such as $Mg_3(VO_4)_2$, $BaWO_4$, Mg_2SiO_4, Zn_2SiO_4, $LiMgPO_4$, $Li_2Mg_3SnO_6$, Mg_2TiO_4, $Mg_2B_2O_6$, and $LiMg_2TiO_5$ [16–24], to near zero. $Ba_5Si_8O_{21}$ and $CaSnSiO_5$ can also adjust τ_f of $BaSi_2O_5$ and $BaAl_2Si_2O_8$ to near zero, respectively [9,25]. However, these regulators often have too small a τ_f value with limited adjustability, or they are expensive and toxic, making it difficult to meet practical application needs.

The glaserite-type topology is known for its amazing chemical diversity and structural versatility. The crystal-chemical formula

[1] School of Optical and Electronic Information, Key Lab of Functional Materials for Electronic Information (B) of MOE, Huazhong University of Science and Technology, Wuhan 430074, China. [2] Wenzhou Key Laboratory of Microwave Communication Materials and Devices, Wenzhou Advanced Manufacturing Institute of HUST, Wenzhou 325035, China.

✉ Corresponding author. E-mail: wenlei@hust.edu.cn

Received: September 30, 2024; Revised: November 24, 2024; Accepted: December 16, 2024

can be written as $A_{(□,1)}B_{(□,2)}[M(TO_4)_2]$, as summarized by Lazoryak and Rosica [26,27]. Some typical derivatives of this general formula are presented in Table 2. This type of topology is a layered structure, taking $Ba_3MgSi_2O_8$ as an example. In this structure, corner-sharing [SiO_4] tetrahedra and [MgO_6] octahedra are polymerized to form the [$Mg(SiO_4)_2$] layer, and the free tetrahedral apexes point outside the layer toward the interlayer space, as shown in Fig. 1. Between the layers, two kinds of interlayer cationic positions are allowed: twelve coordinated positions at the center of the interlayer space (A site) and ten coordinated positions in the layer pockets (B site). The multiplicity of the latter is always twice that of the former. Recently, several related structures have been reported due to the low cost and excellent microwave dielectric properties of alkaline earth silicates [28–32]. The microwave dielectric properties of $Ca_3MgSi_2O_8$ (merwinite) single-phase ceramics were reported by Bafrooei [33] and Zhang [34], who reported good low-ε_r microwave dielectric properties, albeit with negative τ_f values (from −62.9 to −48.4 ppm/°C). Additionally, a $Sr_3MgSi_2O_8$ ceramic was reported by He [35], with a τ_f value of −57.4 ppm/°C.

In this study, we reported the anomalous dielectric characteristics of the $Ba_{3-x}Sr_xMgSi_2O_8$ solid solution and further explained this abnormal behavior through investigation of its crystal structure. Understanding this behavior and the associated regulatory strategies can facilitate the design of more temperature-stable composite ceramic materials in the future.

2 Experimental

Reagent-grade starting materials of $BaCO_3$ (99.8%), $SrCO_3$ (99.8%), $Mg(OH)_2{\cdot}4MgCO_3{\cdot}5H_2O$ (99%), and SiO_2 (99.9%) (Aladdin Industrial Co., China) were weighed according to the stoichiometric ratios of $Ba_{3-x}Sr_xMgSi_2O_8$. The mixtures were subsequently ball-milled separately in a polyethylene jar for 4 h via ZrO_2 balls with distilled water. After drying at 120 °C, the mixtures were calcined in air at 1200 °C for 3 h at a heating rate of 5 °C/min. Then, the calcined powder was ball milled for 4 h and dried. A polyvinyl alcohol solution (5 wt%) was added, and the dried powders were uniaxially pressed into cylindrical samples (12 mm × 6 mm in diameter and height) under 150 MPa. The samples were sintered in the temperature range of 1300–1500 °C for 5 h at a heating rate of 5 °C/min.

The XRD data were obtained via an X-ray diffractometer (D8 Advance, Bruker, Germany) with CuKα radiation. The crystal structures and phase compositions were determined via Rietveld refinement using the FullProf software [36,37]. *In situ* Raman spectra were obtained via an integral Raman microscope (HR-800 LabRaman, Horiba Jobin Yvon, France) equipped with a Linkam heated-cooled device. Thermal etching was performed for 30 min at 75 °C below the optimal sintering temperature to obtain better observations of the grain morphology. The thermally etched surfaces were observed via a scanning electron microscope (GeminiSEM300, Zeiss, Germany). Thermogravimetric analysis (TGA) and differential scanning calorimetry (DSC) were performed via a comprehensive thermal analyzer (STA449F3, Netzsch, Germany) in air between 25 and 1300 °C. ε_r as a function of temperature was obtained via an impedance analyzer (4294A, Agilent Technologies, USA) and a measuring system (VDMS2000, Partulab, China). The samples were polished to approximately 300 μm and coated with 10 mm diameter Ag electrodes for electrical measurement. The density of all the samples was measured via Archimedes' method. ε_r and unloaded $Q{\times}f$ values were measured in the microwave frequency range of

Table 1 Microwave dielectric properties of some low-ε_r ceramics with abnormally positive τ_f values

Ceramic composition	ε_r	$Q{\times}f$ (GHz)	τ_f (ppm/°C)	Ref.
$Ba_5Si_8O_{21}$	7.3	16,700	+25.0	[9]
$A_3(VO_4)_2$ (A = Ba, Sr)	11.0–12.2	44,340–62,347	+28.8±63.5	[10,11]
$CaSnSiO_5$	9.1	61,000	+35.0	[12]
$Mg_3Y_2Ge_3O_{12}$	14.1	12,600	+120.5	[13]
$Ba_9Y_2Si_6O_{21}$	14.9	22,440	+35.8	[14]
Li_2BO_3 (B = Zr, Sn)	12.8–14.1	17,600–20,800	+26.9±39.3	[15]

Table 2 Derivatives of general formula $A_{(□,1)}B_{(□,2)}[M(TO_4)_2]$ by specificity and occupancy of cationic positions (A, B, M, and T) [27]

No.	General formula	Condition	Example	
			Long formula	Short formula
1	$AB_2[M(TO_4)_2]$	$A{\neq}B{\neq}M{\neq}T$	$BaNa_2[Mg(PO_4)_2]$	$BaNa_2Mg(PO_4)_2$
2	$AB_2[M(TO_4)_2]$	$A{=}B{\neq}M{\neq}T$	$AgAg_2[Fe(VO_4)_2]$	$Ag_3Fe(VO_4)_2$
3	$AB_2[M(TO_4)_2]$	$A{\neq}B$, $A{=}M$, $B{\neq}M{\neq}T$	$NaK_2[Na(SO_4)_2]$	$KNaSO_4$
4	$AB_□[M(TO_4)_2]$	$A{\neq}M{\neq}T$, $B{=}0$	$Rb□[Fe(MoO_4)_2]$	$RbFe(MoO_4)_2$
5	$(A1,A2)B_□[M(TO_4)_2]$	$A1{\neq}A2{\neq}M{\neq}T$, $B{=}0$	$(Ba_{0.3}Sr_{0.7})□[Zr(PO_4)_2]$	$Ba_{0.3}Sr_{0.7}Zr(PO_4)_2$
6	$A(B1,B2)[M(TO_4)_2]$	$A{=}B1{\neq}B2$, $B2{=}M{\neq}T$	$Ba(Ba_{0.5}Na_{0.5})_2[Na(PO_4)_2]$	$BaNaPO_4$
7	$A_□B_2[M(TO_4)_2]$	$B{\neq}M{\neq}T$, $A{=}0$	$□K_2[Zr(PO_4)_2]$	$K_2Zr(PO_4)_2$
8	$A_□B_□[M(TO_4)_2]$	$M{\neq}T$, $A{=}0$, $B{=}0$	$□□[Ni(ReO_4)_2]$	$Ni(ReO_4)_2$
9	$A_□B_□[M(T1,T2O_4)_2]$	$M{\neq}T1{\neq}T2$, $A{=}0$, $B{=}0$	$□□[Zr(Mo_{0.5}W_{0.5}O_4)_2]$	$Zr(Mo_{0.5}W_{0.5}O_4)_2$
10	$AB_□[(M1,M2)(TO_4)_2]$	$A{\neq}M1{\neq}M2{\neq}T$, $B{=}0$	$K□[(Mg_{0.5}Zr_{0.5})(MoO_4)_2]$	$K(Mg_{0.5}Zr_{0.5})(MoO_4)_2$
11	$AB_2[M(TO_4)_2]$	$A{=}B{=}M{\neq}T$	$TlTl_2[Tl(WO_4)_2]$	Tl_2WO_4
12	$AB_2H[M(TO_4)_2]$	$A{=}B{\neq}M{\neq}T$	$NaNa_2H[Mg(PO_4)_2]$	$Na_3HMg(PO_4)_2$
13	$AB_□H[M(TO_4)_2]$	$A{\neq}M{\neq}T$, $B{=}0$	$K□H[Zr(PO_4)_2]$	$KHZr(PO_4)_2$

Note: □ refers to the structural vacancies in the crystal-chemical formula.

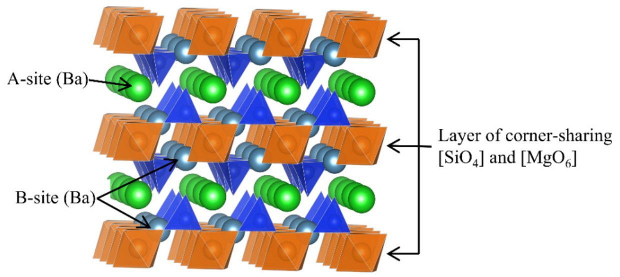

Fig. 1 Crystal structure of $Ba_3MgSi_2O_8$ illustrated with $[SiO_4]$ tetrahedra and $[MgO_6]$ octahedra.

8–13 GHz in the TE_{011} mode via the parallel plate cavity method using a vector network analyzer (Agilent E8362B, Agilent Technologies, USA) and parallel silver boards [38,39]. The τ_f value was calculated in the temperature range of 25–85 °C.

Density functional theory (DFT) calculations were performed via the Vienna ab initio simulation package (VASP) [40]. The cutoff energy of the plane wave was set to 520 eV. The Γ-centered k-meshes were 2 × 2 × 2 for $Ba_3MgSi_2O_8$, 3 × 3 × 2 for $BaSr_2MgSi_2O_8$, and 2 × 3 × 2 for $Sr_3MgSi_2O_8$. The total energy of the systems converged to 10^{-6} eV, and the force acting on each atom in the structural relaxation converged to 0.01 eV/Å. Vibrational modes were obtained from frequency calculations via the density functional perturbation theory method [41], with a more stringent energy convergence criterion of 10^{-8} eV. The Raman activity of the vibrational modes was subsequently identified via the Phononpy code [42,43].

The formation energy was calculated via Eq. (1):

$$E_{\text{form}} = E_{A_mB_n} - \sum_{i\in(A,B)} n_iE_i \tag{1}$$

where E_{form}, $E_{A_mB_n}$, and E_i are the formation energy, the energy of the compound A_mB_n, and that of the atom i within its most stable simple substance, respectively [44,45]. n_i is the amount of the atom i. Additionally, the formation energy for the doped systems was calculated via Eq. (2):

$$E_{\text{form}} = E_{\text{sub}} - E_{\text{unsub}} - \sum_i n_iE_i \tag{2}$$

where E_{sub} (E_{unsub}) represents the energy of the substituted (unsubstituted) system, E_i denotes the energy of the substitution atom or the substituted atom, and n_i indicates the number of substitutions [46]. The value of n_i is positive for substitution atoms and negative for substituted atoms. The k-point sampling density in the first Brillouin zone was set to 0.02×2π $Å^{-1}$ for all these systems, except for the oxygen atom. The energy of the oxygen atoms was calculated via the spin-triplet state of the oxygen molecule, which was placed in a 10 Å × 10 Å × 10 Å box with only the Γ point.

3 Results and discussion

3.1 Crystal structural analysis of $Ba_{3-x}Sr_xMgSi_2O_8$ ceramics

The XRD patterns of the $Ba_{3-x}Sr_xMgSi_2O_8$ ceramics are shown in Fig. 2(a). All the curves in the XRD pattern show similar crystal structures. With increasing x, the XRD peak moves to a higher

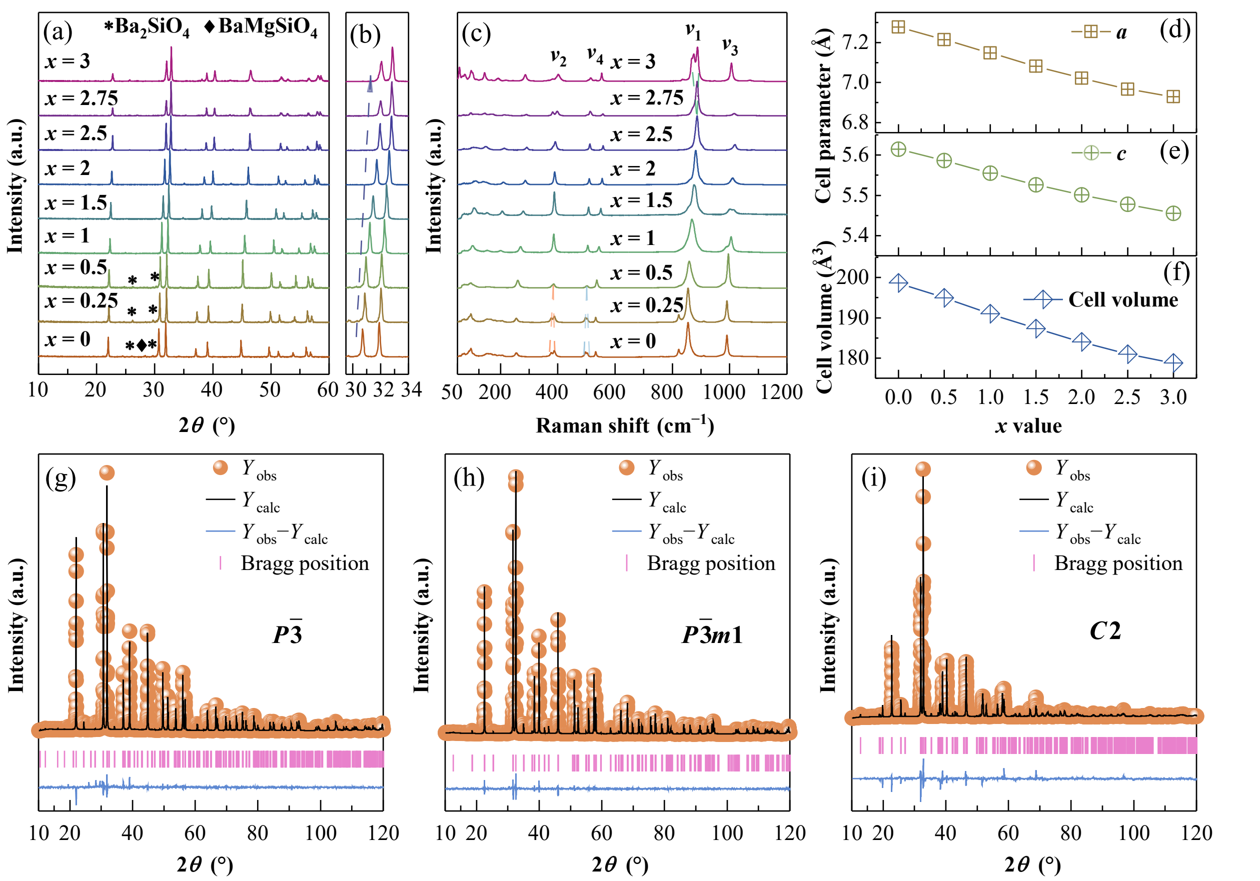

Fig. 2 (a) XRD patterns of $Ba_{3-x}Sr_xMgSi_2O_8$ ($0 \le x \le 3$) ceramics sintered at optimized temperature, (b) locally enlarged diffraction peaks in the angle range of 30°–34°. (c) Room-temperature Raman spectra of $Ba_{3-x}Sr_xMgSi_2O_8$ ($0 \le x \le 3$) samples. Unit-cell parameters and unit-cell volume, which were converted to $Z = 1$ crystal structure as a function of Sr content: (d) cell parameter a, (e) cell parameter c, (f) cell volume. XRD refinements for various $Ba_{3-x}Sr_xMgSi_2O_8$ samples: (g) $x = 0$, (h) $x = 2$, and (i) $x = 3$.

angle, indicating that Sr^{2+} ions enter the crystal structure to replace Ba^{2+} ions and form a solid solution. For the Ba-rich group (i, $x \leq 0.5$), the peaks were indexed with trigonal cells of a = 9.7 Å and c= 7.2 Å. When $x \leq 0.5$, very weak diffraction peaks at 26.1°, 29.6°, and 28.2° were observed, which belong to $BaMgSiO_4$ (ICDD#16-0573) and Ba_2SiO_4 (ICDD#70-2113). For the samples in group (ii, $0.5 < x < 2.5$), the peaks were indexed with trigonal cells of a = 5.5 Å and c = 7.0 Å. The cell volume of group (i) was approximately three times larger than that of group (ii). For the Sr-rich group (iii; $x \geq 2.5$), all the diffraction peaks were successfully indexed with monoclinic cells of a = 9.4 Å, b = 5.5 Å, and c = 13.9 Å, the volume of which was approximately four times larger than that of the former group (ii). This result is consistent with previous research [47,48]. The Raman spectra of the $Ba_{3-x}Sr_xMgSi_2O_8$ ceramics are shown in Fig. 2(c). The intense peaks at approximately 880, 400, 1000, and 550 cm^{-1} are attributed to the four normal modes of [SiO_4] tetrahedra: symmetric-stretching vibrations (v_1), symmetric-bending vibrations (v_2), asymmetric-stretching vibrations (v_3), and asymmetric-bending vibrations (v_4), respectively [49]. As x increased, an overall shift of the peak was observed, indicating that the crystal structure deformed continuously. Some vibrational modes split when $x \geq 2.5$ (v_1, v_2) and $x \leq 0.5$ (v_2, v_4), which is related to the resolving of vibrational degeneracy associated with symmetry reduction. To determine the crystal structure of the samples, Rietveld refinement was performed, which is shown in Figs. 2(h) and 2(i) and Table S1 in the Electronic Supplementary Material (ESM). The initial models were consistent with the literature reports to facilitate the analysis [47,48,50]. Following standard crystallographic conventions, the cell parameters are $a_{ii} = b_{iii} = a_i/\sqrt{3}$, $c_{ii} = c_{iii}\sin\beta/2 = c_i$ (subscript "i", "ii", and "iii" indicates the trigonal cell (Z = 3) of group (i), trigonal cell (Z = 1) of group (ii), and monoclinic cell (Z = 4) of group (iii), respectively). As x increases, the cell volume and lattice parameters of a and c decrease monotonically, as shown in Figs. 2(d)–2(f). The observed variation in the unit cell volume aligns with the findings derived from the XRD patterns. This alteration can be attributed to the smaller ionic radius of Sr^{2+} ions (1.31 Å) than that of Ba^{2+} ions (1.61 Å), with a coordination number of 12 [51].

The change in the structure caused by Sr replacement is illustrated in Fig. 3. Within the glaserite-type structure, the $P\bar{3}m1$ space group represents the highest symmetry, as depicted in Figs. 3(b) and 3(e). When x = 0, the interlayer positions are occupied by Ba^{2+} ions. The relatively large Ba^{2+} ions were compelled to occupy the smaller B positions, which induced structural distortion. In the $P\bar{3}$ model, Ba^{2+} ions occupy three kinds of crystallographic positions: Ba1 with six coordination positions, Ba2 with nine coordination positions, and Ba3 with ten coordination positions. [SiO_4] tetrahedra tilted to different orientations, as shown in Figs. 3(a) and 3(d). The structure is inherently unstable, which results in the presence of the inevitable secondary phase [47,52]. As x increases, the proportion of the secondary phase diminishes gradually. A transition in the space group occurs at approximately x = 0.5, resulting in the synthesis of a pure phase. In group (ii), Sr^{2+} ions preferentially occupy the B positions, as corroborated by the refinement results. For x = 2, nearly all the A-sites are occupied by Ba^{2+} ions, whereas the B-sites are occupied by Sr^{2+} ions. With further increases in x, Sr^{2+} ions are compelled to occupy the A positions, leading to a decrease in the interlayer spacing. At approximately x = 2.5, a change in symmetry is observed. For x = 3, the layers become misaligned, and the [SiO_4] tetrahedra tilt in alternating interlayer spaces to accommodate the smaller Sr^{2+} ions in the $C2$ model [47,53]. Nevertheless, the overall order of the alternation of cations and anions remains unchanged, as illustrated in Figs. 3(c) and 3(f).

3.2 Microstructure and microwave dielectric properties of $Ba_{3-x}Sr_xMgSi_2O_8$ ceramics

The microstructures and relative densities of the sintered samples are presented in Fig. 4. SEM observations revealed dense microstructures in the $Ba_{3-x}Sr_xMgSi_2O_8$ ceramics. Among these ceramics, the $Ba_3MgSi_2O_8$ ceramic has the lowest density, which

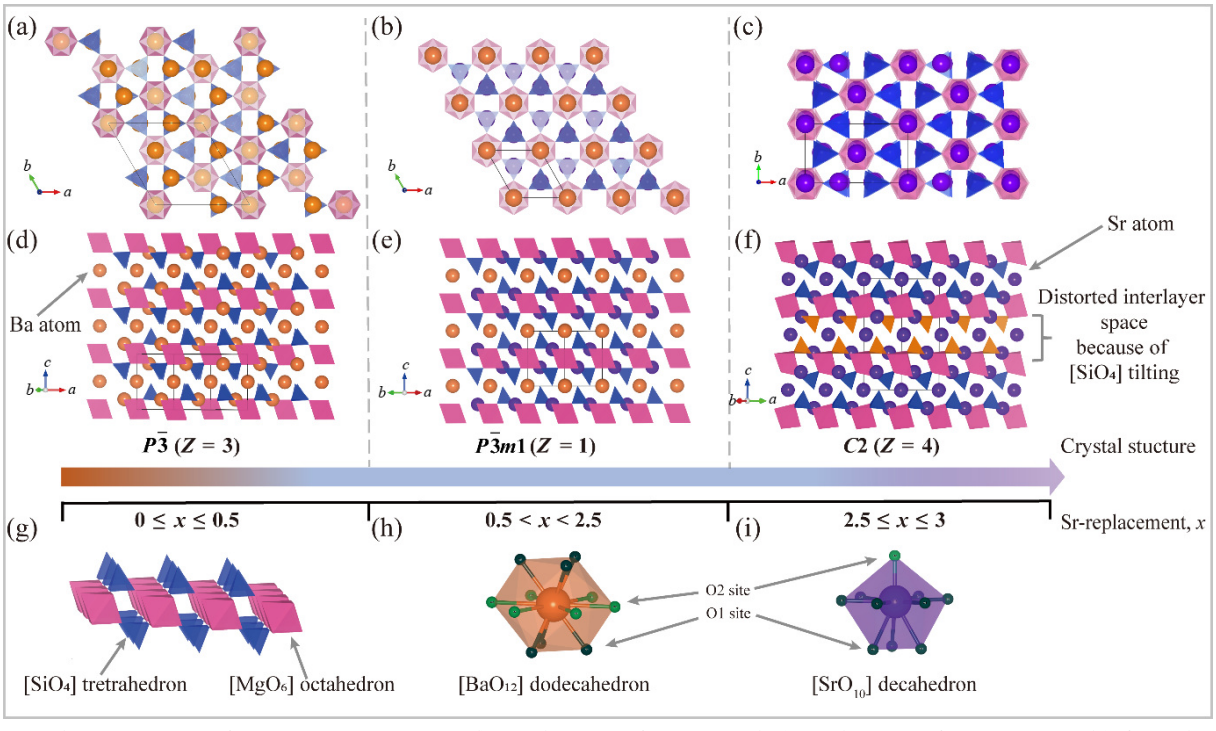

Fig. 3 Crystal structure patterns of $Ba_{3-x}Sr_xMgSi_2O_8$ ceramics: (a, d) Crystal structure of $Ba_3MgSi_2O_8$, (b, e) crystal structure of $BaSr_2MgSi_2O_8$, and (c, f) crystal structure of $Sr_3MgSi_2O_8$. (g) Framework of a single layer in $BaSr_2MgSi_2O_8$. (h) [BaO_{12}] dodecahedron and (i) [SrO_{10}] decahedron environments in $BaSr_2MgSi_2O_8$.

may be attributed to the very narrow densification temperature range below 1295 °C [48]. For the Ba-rich group ($x \leq 0.5$) and Sr-rich group ($x \geq 2.5$), anisotropic grain growth is observed, which may be related to their low structural symmetry, such as that of Fe_2O_3-doped mullite [54] and β-Al_2TiO_5 [55]. The substitution of Sr^{2+} ions for Ba^{2+} ions results in an approximately linear increase in the sintering temperature and a decrease in the grain size for the group ($0.5 < x < 2.5$).

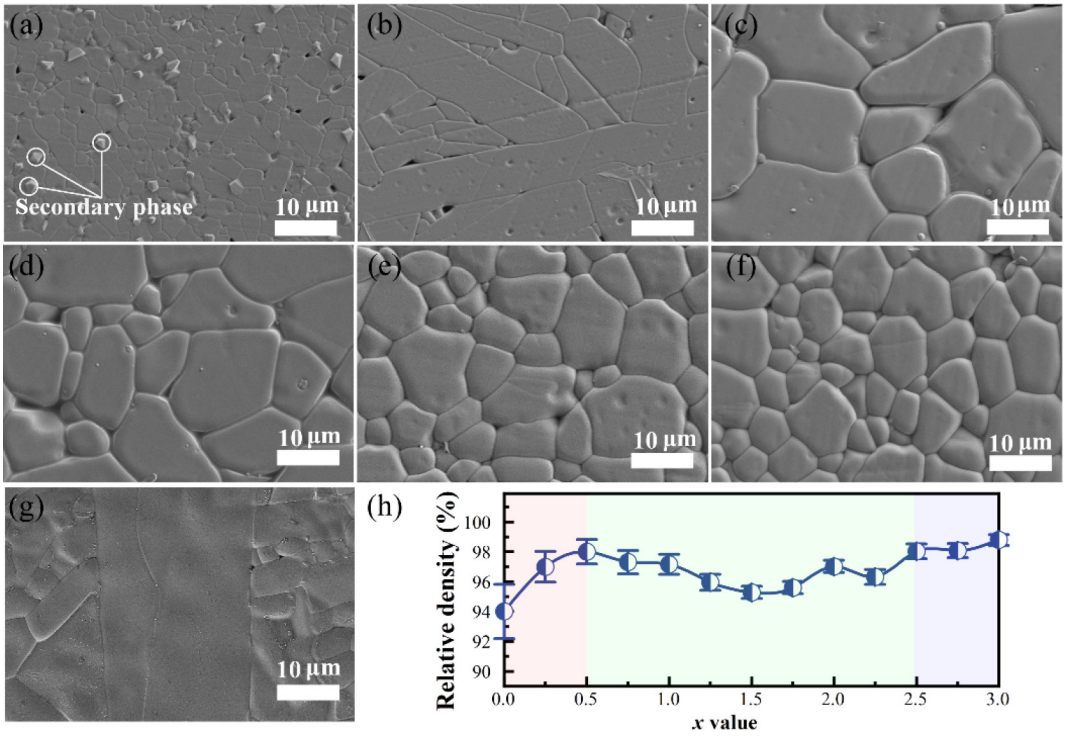

Fig. 4 SEM images of thermally etched surfaces: (a) $x = 0$, 1300 °C, (b) $x = 0.5$, 1350 °C, (c) $x = 1$, 1375 °C, (d) $x = 1.5$, 1400 °C, (e) $x = 2$, 1425 °C, (f) $x = 2.5$, 1450 °C, (g) $x = 3$, 1500 °C. (h) Relative density as a function of x value.

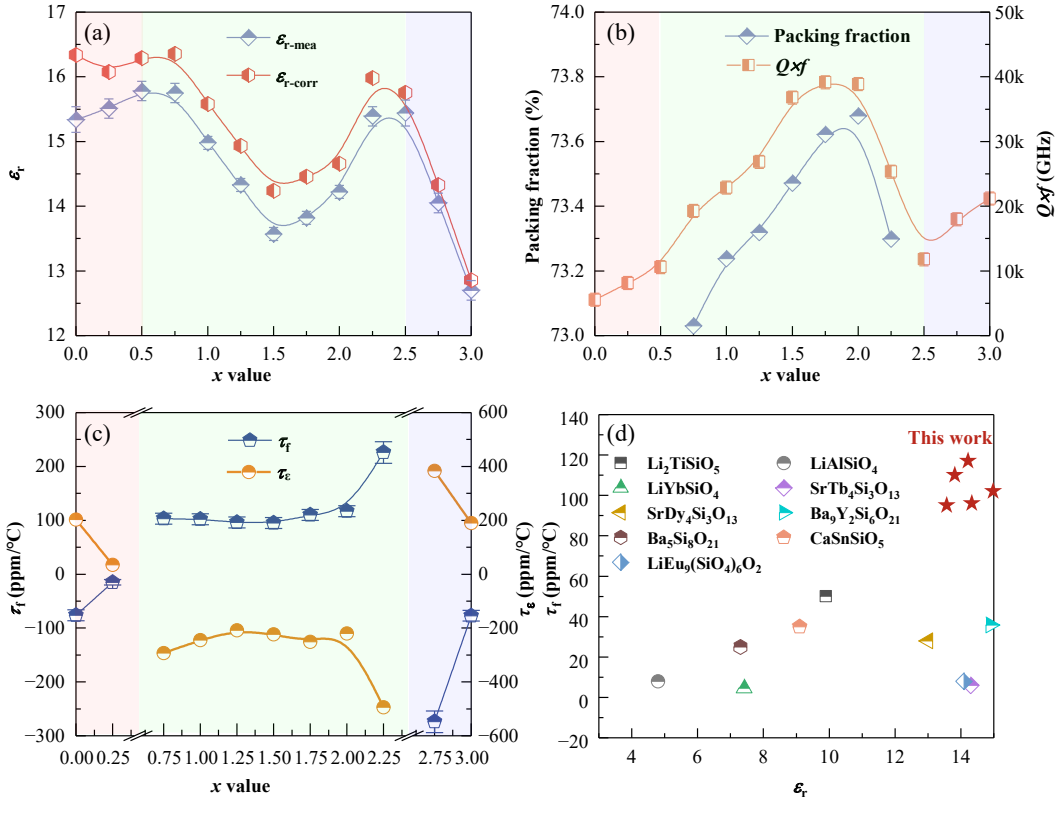

Fig. 5 Microwave dielectric properties of $Ba_{3-x}Sr_xMgSi_2O_8$ ceramics: (a) ε_r, (b) packing fraction and $Q \times f$ value, (c) τ_f and τ_ε values, (d) summary of low-ε_r silicate microwave dielectric ceramics with anomalous τ_f values, where $\varepsilon_{r\text{-corr}}$ is the relative permittivity of the material corrected for porosity, and $\varepsilon_{r\text{-mea}}$ is the actual measurement value.

The microwave dielectric properties versus the x value of the $Ba_{3-x}Sr_xMgSi_2O_8$ ceramics are presented in Fig. 5. The impact of porosity on ε_r is evaluated via Bosman and Havinga's method. $\varepsilon_{r\text{-corr}}$ is the relative permittivity of the material corrected for porosity and $\varepsilon_{r\text{-mea}}$ is the actual measurement value. $Ba_3MgSi_2O_8$ has a large intrinsic ε_r, which can be attributed to the greater ionic polarizability of Ba^{2+} (6.40 Å^3) [56,57]. To further investigate the relationship between permittivity and polarization, the Clausius–Mossotti (C–M) equation was used, as shown in Fig. S1 in the ESM. The ion polarizability per unit volume calculated from Shannon's additive rule is distributed linearly [58]. However, with increasing x value, the measured ε_r has a bimodal distribution, peaking in the phase transition regions (x = 0.5, x = 2.5). This is due to the phase transformation coupled to the optical mode, which is predicted by the classical Lyddane–Sach–Teller (LST) relation [59,60]. The data indicate that ε_r of this ceramic was mainly dominated by structural changes. This observation also aligns with the results of the temperature-dependent dielectric spectra, as shown in Fig. 6, which is consistent with the behavior observed in the $BiVO_4$-based monoclinic scheelite solid-solution ceramics [61,62]. In the green region, the $Q\times f$ value reaches its maximum value ranging from 36,804 to 39,419 GHz when x = 1.5–2. It has been reported that the $Q\times f$ value can be evaluated with the packing fraction [63–65]. For the $P\bar{3}m1$ structure, the packing fraction is defined as Eq. (3):

$$\text{Packing fraction} = \frac{3\pi/4 \times (3r^3_{(Ba/Sr)} + r^3_{Mg} + 2r^3_{Si} + 8r^3_{O})}{V_{cell}} \times Z \quad (3)$$

where $r_{(Ba/Sr)}$, r_{Mg}, r_{Si}, and r_O are the effective ionic radii at each coordination number, V_{cell} is the volume of the primitive unit cell, and Z = 1. The variation in the $Q\times f$ value of the samples in group (ii) resembles the packing fraction, as shown in Fig. 5(b). This is because of the decreased lattice vibration with an increased packing fraction, thereby reducing the intrinsic loss [63]. τ_f is sensitive to structural transitions [66–68]. Moreover, in the present study, all the samples have positive τ_f values and large negative τ_ε values in group (ii), as demonstrated in Fig. 5(c). The τ_f value initially decreased within the range of $0.75 \le x \le 1.5$, followed by an increase in the range of $1.5 \le x \le 2.25$. The minimum τ_f value, with a mean of 95 ppm/°C, was observed at x = 1.5. For $x > 2$ in group (ii), a significant increase in the τ_f value was noted, where τ_f was adjusted to +226 ppm/°C at x = 2.25. However, this increase in τ_f was associated with a reduction in the $Q\times f$ value and an increase in ε_r [69]. Overall, optimal microwave dielectric properties were attained at x = 2 with $\varepsilon_r \approx$ 14.2, $Q\times f \approx$ 38,900 GHz, and $\tau_f \approx$ +117 ppm/°C. Figure 5(d) presents a performance comparison of silicate microwave dielectric ceramics with anomalous τ_f values [12,14,70–75].

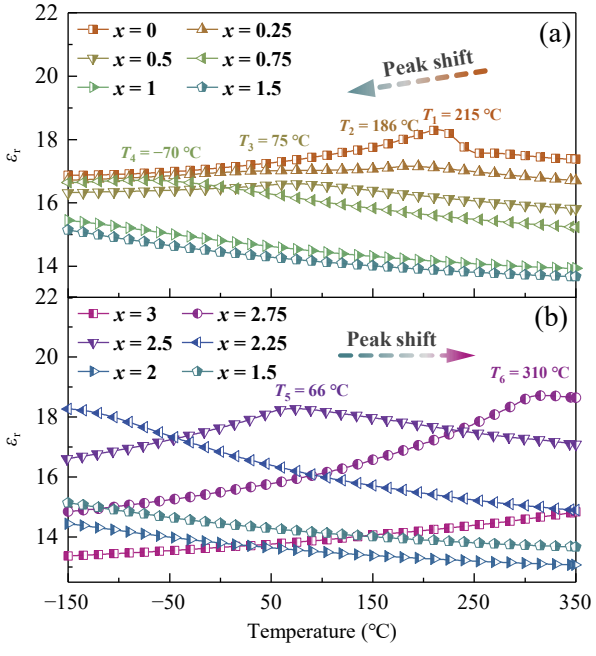

Fig. 6 ε_r of $Ba_{3-x}Sr_xMgSi_2O_8$ ceramics as a function of temperature at 1 MHz: (a) $0 \le x \le 1.5$; (b) $1.5 \le x \le 3$ where T_1–T_6 denote the temperatures associated with the permittivity peaks, which are categorized by the same color.

To comprehensively understand the impact of Sr substitution on the dielectric performance of $Ba_{3-x}Sr_xMgSi_2O_8$ ceramics, measurements of their temperature-dependent dielectric properties were conducted. ε_r as a function of temperature distinctly illustrates the dependence relationship of the permittivity peak with the composition (Fig. 6). T_1–T_6 denote the temperatures associated with the permittivity peaks, which are categorized by the same color. With increasing Sr^{2+} content, the phase transition temperature of the $Ba_{3-x}Sr_xMgSi_2O_8$ ceramics shifts from 215 °C to below −150 °C within the range of $0 \le x \le 1$. Furthermore, the phase transition peak changes from below −150 to 593 °C in the range of $2.25 \le x \le 3$, as depicted in Fig. 6 and Fig. S2 in the ESM.

3.3 Thermal, lattice vibration, and DFT calculations of $Ba_{3-x}Sr_xMgSi_2O_8$ ceramics

Raman spectroscopy is an effective method for observing slight changes in the crystal structure of solid materials. As the temperature increases, the Raman peaks systematically broaden, suggesting an increase in the average bond length and widening of the distribution of average bond lengths and angles, which reflects a greater degree of crystal vibration disorder in the structure. The *in situ* XRD patterns illustrate that all the peaks shift to the left as the temperature increases, indicating a systematic increase in the cell parameters [65], as shown in Fig. 7. For the sample of x = 0, the merging of the ν_2 mode and ν_4 mode occurs at 200–300 °C, which may be due to the tilting of Si–O dangling bonds in response to temperature variations [47]. This phenomenon indicates a structural change that could be associated with the peak observed in ε_r as a function of the temperature in Fig. 6. For the sample of x = 3, the continuous merging of Raman peaks from −150 to 400 °C signifies persistent structural deformation, whereas the XRD peaks reveal phase transitions occurring up to 700 °C. This behavior is likely a consequence of the excessively small size of the A-site ions, causing tilting and symmetry loss of the SiO_4 tetrahedra. This indicates that $Sr_3MgSi_2O_8$ is significantly distorted at room temperature. This distortion may account for the high chi-square value of the refinement result, irrespective of whether the $P21/a$ model or the $C2$ model is employed [47,52,76]. However, in the case of the sample of x = 2, a comparison with the other two structures reveals no significant changes in the X-ray diffraction (XRD) peaks and Raman vibrational modes from room temperature to 400 °C. This observation indicates a relatively stable lattice structure.

To understand the phase behavior during the synthesis and sintering processes, TGA and DSC tests were performed, as illustrated in Fig. S3 in the ESM. In the TGA test, three notable weight loss steps were observed, which corresponded to the decomposition of the crystallization water (230 °C), $MgCO_3$ (440 °C), $BaCO_3$ (850 °C) and $SrCO_3$ (945 °C) [77,78]. The earlier endothermic peaks observed in the DSC curve suggest that the

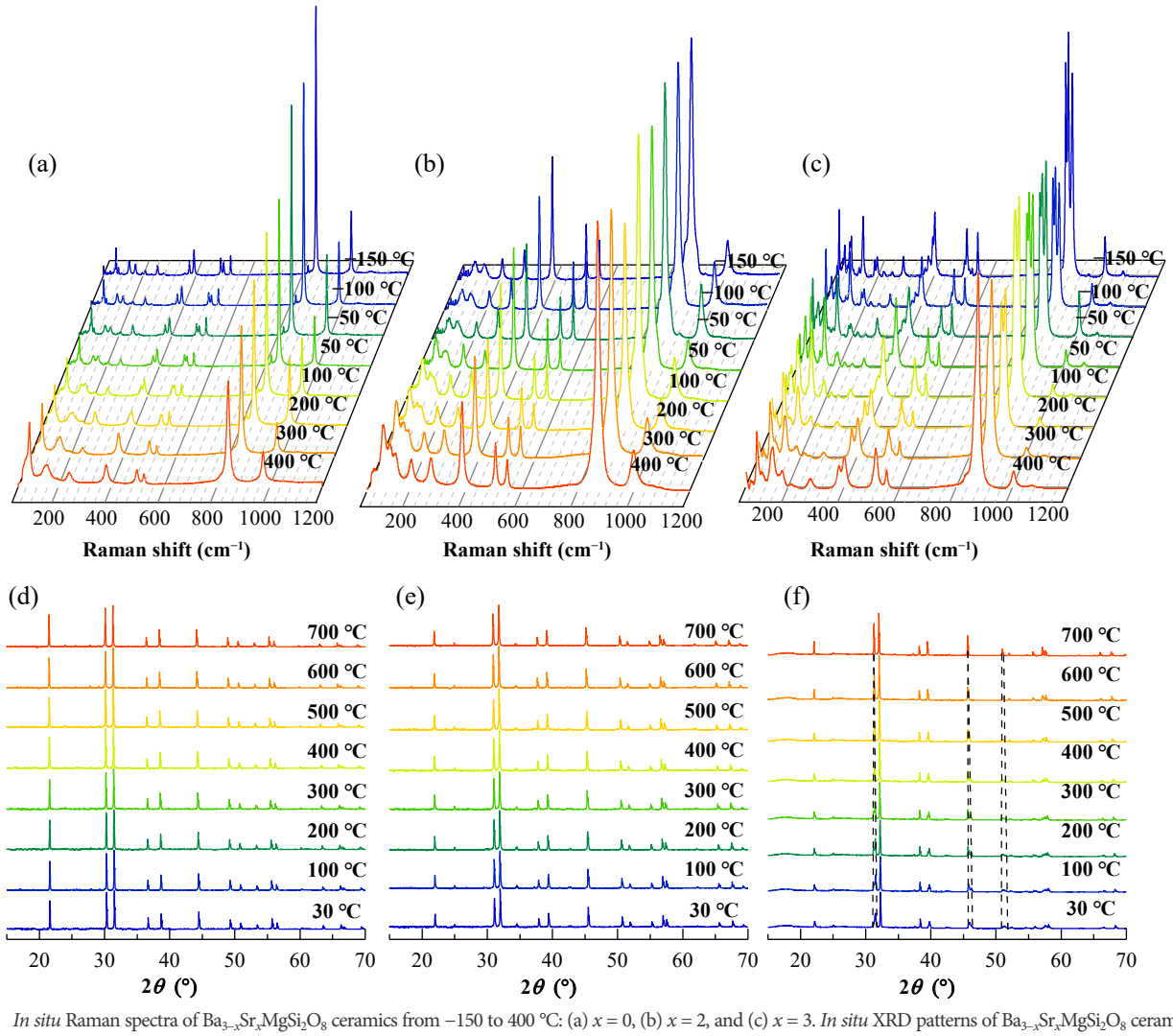

Fig. 7 *In situ* Raman spectra of $Ba_{3-x}Sr_xMgSi_2O_8$ ceramics from −150 to 400 °C: (a) $x = 0$, (b) $x = 2$, and (c) $x = 3$. *In situ* XRD patterns of $Ba_{3-x}Sr_xMgSi_2O_8$ ceramics of 30 to 700 °C: (d) $x = 0$, (e) $x = 2$, and (f) $x = 3$.

synthesis temperature of the phases decreases with increasing Sr content. Figures 8(a)–8(g) and Figs. S4 and S5 in the ESM depict the symmetry coordinates of the Raman peaks associated with the normal modes of [SiO_4] tetrahedra within the $Ba_{3-x}Sr_xMgSi_2O_8$ ceramic, as previously described. The formation energy of the $Ba_{3-x}Sr_xMgSi_2O_8$ ceramics ($x = 0$, 2, 3) is illustrated in Fig. 8(h). An analysis of the formation energies across the three structural variants revealed that the $P\bar{3}m1$ model with the highest symmetry is the most easily synthesized and demonstrates the greatest stability. In the second step of the calculations, the same structural model $P\bar{3}m1$ was employed to maintain accuracy. The formation energy difference between the structure with the A site partially substituted by 12.5% Sr^{2+} ions and the structure with preferential occupancy is 4 meV. Conversely, when the 12.5% Ba^{2+} ions are constrained to be embedded in the layer pocket B position, the formation energy difference from the ideal composition is 126 meV, as shown in Fig. 8(i). The observed variations in formation energy between the unsubstituted model and the models with different substitution ratios indicate a tendency for preferential occupancy within the $Ba_{3-x}Sr_xMgSi_2O_8$ ceramics. The DFT simulation data align with the refinement results, demonstrating that such occupancy can effectively reduce the formation energy of the system [27,79]. This reduction may account for the highest packing fraction observed at $x = 2$, as it mitigates size mismatch at the interlayer positions.

4 Conclusions

$Ba_{3-x}Sr_xMgSi_2O_8$ solid solution with abnormal dielectric behavior was successfully prepared via an ion substitution design. With increasing Sr content with decreasing radius, the second phase disappears ($x > 0.5$), and a solid solution forms. The phase transitions of $P\bar{3}$ to $P\bar{3}m1$ and $P\bar{3}m1$ to $C2$ were clearly observed in compositions near $x = 0.5$ and $x = 2.5$ with the support of *in situ* XRD and *in situ* Raman spectroscopy. ε_r is dominated by structural changes, and peak values are observed at the phase transition compositions. The $Q\times f$ value of a sample is related to the packing fraction, which indicates that the intrinsic dielectric loss caused by the damping of lattice vibrations is the main influencing mechanism. The τ_f and τ_ε values are mainly determined by phase change factors, and the ε_r peaks, as a function of temperature, were adjusted from high temperature to low temperature and then returned to high temperature through an ion substitution design. The compositional series ($1 \le x \le 2$) displayed exceptional performance, including low ε_r values ranging from 13.57 to 14.98, high $Q\times f$ values (22,873–39,149 GHz) and positive τ_f values ((+95)–(+117) ppm/°C). The optimal microwave dielectric properties could be achieved in the ideal stoichiometric $BaSr_2MgSi_2O_8$ with $\varepsilon_r \approx 14.2$, $Q\times f \approx 38{,}900$ GHz, and $\tau_f \approx +117$ ppm/°C. With the support of DFT simulations, different Raman peak symmetry coordinates were identified. The difference in formation energy demonstrated that Sr^{2+} ions tend to

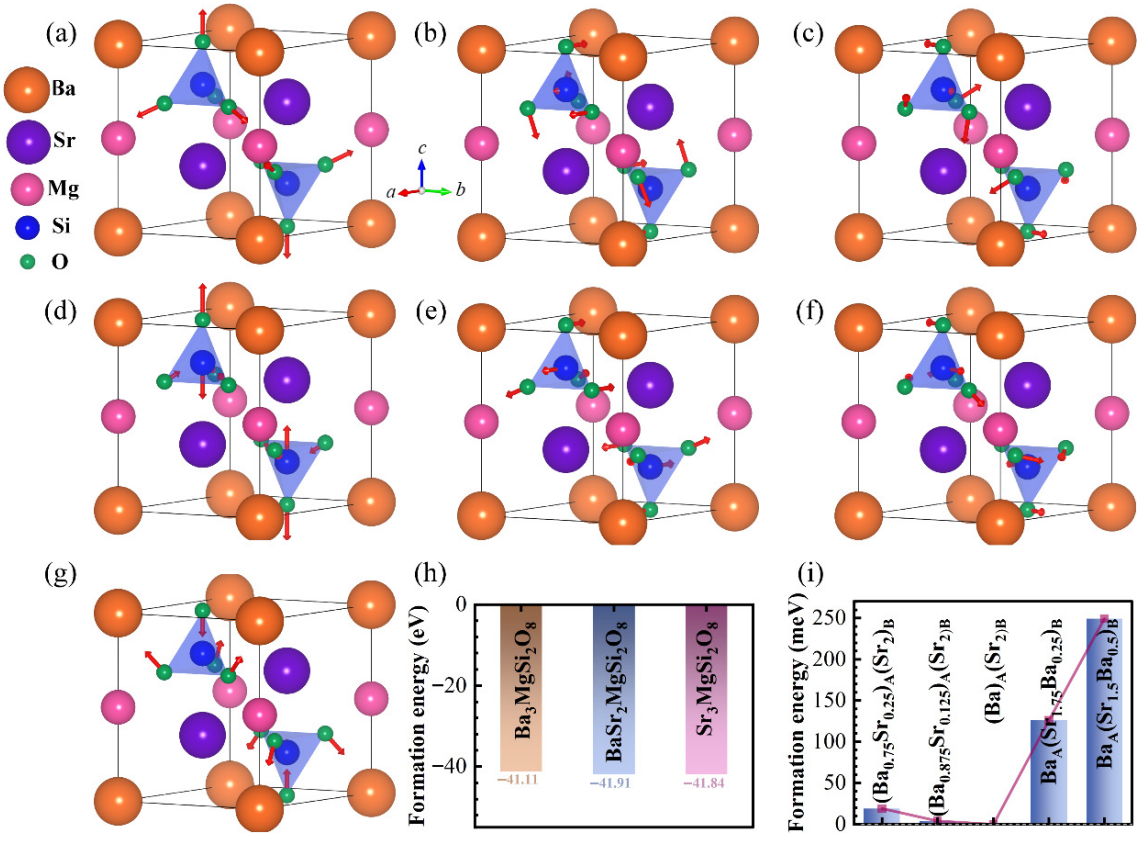

Fig. 8 Cell of $BaSr_2MgSi_2O_8$ material: (a) symmetric-stretching vibrations ν_1 near 880 cm^{-1}, (b, c) symmetric-bending vibrations ν_2 near 390 cm^{-1}, (d) asymmetric stretching vibrations ν_3 near 1010 cm^{-1}, (e–g) asymmetric-bending vibrations ν_4 near 510 and 555 cm^{-1}, (h) formation energy of $Ba_{3-x}Sr_xMgSi_2O_8$ (x = 0, 2, 3), (i) formation energy of models with interlayer A positions partially occupied by Sr^{2+} ions and interlayer positions partially occupied by Ba^{2+} ions.

occupy the interlayer B sites, thereby reducing the ionic size mismatch within the crystal structure. In summary, this research not only contributes to the fundamental understanding of $Ba_{3-x}Sr_xMgSi_2O_8$ ceramics but also lays the foundation for future innovations in designing low-ε_r composite ceramics with near-zero τ_f values.

Acknowledgements

This work was supported by the National Natural Science Foundation of China (Nos. NSFC-52072133 and 52302140), Joint Funds of the National Natural Science Foundation of China-Key Program (No. U21B2068), and Major Scientific and Technological Innovation Project of Wenzhou (No. ZG2023040). The authors are grateful to the Analytical and Testing Center, Huazhong University of Science and Technology, for SEM analyses.

Declaration of competing interest

The authors have no competing interests to declare that are relevant to the content of this article.

Electronic Supplementary Material

Supplementary material is available in the online version of this article at https://doi.org/10.26599/JAC.2024.9221020.

References

[1] Reaney IM, Iddles D. Microwave dielectric ceramics for resonators and filters in mobile phone networks. *J Am Ceram Soc* 2006, **89**: 2063–2072.

[2] Kamutzki F, Schneider S, Barowski J, *et al.* Silicate dielectric ceramics for millimetre wave applications. *J Eur Ceram Soc* 2021, **41**: 3879–3894.

[3] He GQ, Jiang Y, Song KX, *et al.* Ultrahigh-Q $Sr_{1+x}Y_2O_{4+x}$ (x = 0.01–0.04) microwave dielectric ceramics for temperature-stable millimeter-wave dielectric resonator antennas. *J Adv Ceram* 2024, **13**: 155–165.

[4] Hu X, Huang XJ, Chen YH, *et al.* Phase evolution and microwave dielectric properties of $SrTiO_3$ added $ZnAl_2O_4$–Zn_2SiO_4–SiO_2 ceramics. *Ceram Int* 2020, **46**: 7050–7054.

[5] Yokoi A, Ogawa H, Kan A, *et al.* Microwave dielectric properties of $Mg_4Nb_2O_9$–3.0wt% LiF ceramics prepared with $CaTiO_3$ additions. *J Eur Ceram Soc* 2005, **25**: 2871–2875.

[6] Surendran KP, Santha N, Mohanan P, *et al.* Temperature stable low loss ceramic dielectrics in $(1-x)ZnAl_2O_4$–$xTiO_2$ system for microwave substrate applications. *Eur Phys J B Condens Matter Complex Syst* 2004, **41**: 301–306.

[7] Li L, Yang S, Wu SY, *et al.* Nonlinear variation of resonant frequency with temperature and temperature-dependent τ_f in Al_2O_3–TiO_2 microwave dielectric composites. 2021, **118**: 212902.

[8] Kolodiazhnyi T, Annino G, Spreitzer M, *et al.* Development of Al_2O_3–TiO_2 composite ceramics for high-power millimeter-wave applications. *Acta Mater* 2009, **57**: 3402–3409.

[9] Lei W, Zou ZY, Chen ZH, *et al.* Controllable τ_f value of barium silicate microwave dielectric ceramics with different Ba/Si ratios. *J Am Ceram Soc* 2018, **101**: 25–30.

[10] Umemura R, Ogawa H, Yokoi A, *et al.* Low-temperature sintering-microwave dielectric property relations in $Ba_3(VO_4)_2$ ceramic. *J Alloys Compd* 2006, **424**: 388–393.

[11] Cheng K, Li CC, Yin CZ, *et al.* Effects of Sr^{2+} substitution on the crystal structure, Raman spectra, bond valence and microwave dielectric properties of $Ba_{3-x}Sr_x(VO_4)_2$ solid solutions. *J Eur Ceram Soc* 2019, **39**: 3738–3743.

[12] Wu SP, Chen DF, Jiang C, *et al.* Synthesis of monoclinic $CaSnSiO_5$ ceramics and their microwave dielectric properties. *Mater Lett* 2013, **91**: 239–241.

[13] Tang Y, Zhang ZW, Li J, *et al.* $A_3Y_2Ge_3O_{12}$ (A = Ca, Mg): Two novel microwave dielectric ceramics with contrasting τ_f and $Q\times f$. *J Eur Ceram Soc* 2020, **40**: 3989–3995.
[14] Wei JS, Xu ZH, Liu P, *et al.* $Ba_9Y_2Si_6O_{24}$: A new silicate dielectric ceramic for microwave communication application. *Mater Lett* 2016, **178**: 144–146.
[15] Pang LX, Zhou D. Microwave dielectric properties of low-firing Li_2MO_3 (M = Ti, Zr, Sn) ceramics with B_2O_3–CuO addition. *J Am Ceram Soc* 2010, **93**: 3614–3617.
[16] Ogawa H, Yokoi A, Umemura R, *et al.* Microwave dielectric properties of $Mg_3(VO_4)_2$–$xBa_3(VO_4)_2$ ceramics for LTCC with near zero temperature coefficient of resonant frequency. *J Eur Ceram Soc* 2007, **27**: 3099–3104.
[17] Hao Z, Yue ZX, Meng SQ, *et al.* Low -temperature sintering and microwave dielectric properties of $Ba_3(VO_4)_2$–$BaWO_4$ ceramic composites. *J Am Ceram Soc* 2008, **91**: 3738–3741.
[18] Meng SQ, Yue ZX, Zhuang H, *et al.* Microwave dielectric properties of $Ba_3(VO_4)_2$–Mg_2SiO_4 composite ceramics. *J Am Ceram Soc* 2009, **93**: 359–361.
[19] Lv Y, Zuo RZ, Yue ZX. Structure and microwave dielectric properties of $Ba_3(VO_4)_2$–$Zn_{2-x}SiO_{4-x}$ ceramic composites. *Mater Res Bull* 2013, **48**: 2011–2017.
[20] Dong ZW, Zheng Y, Cheng P, *et al.* Microwave dielectric properties of low-temperature sinterable $Ba_3(VO_4)_2$–$LiMgPO_4$ composite ceramics. *Mater Lett* 2014, **131**: 151–153.
[21] Zhang J, Zuo RZ, Song J, *et al.* Low-loss and low-temperature firable $Li_2Mg_3SnO_6$–$Ba_3(VO_4)_2$ microwave dielectric ceramics for LTCC applications. *Ceram Int* 2018, **44**: 2606–2610.
[22] Ding LF, Song MQ, Ma HT. Novel temperature-stable Mg_2TiO_4–$Ba_3(VO_4)_2$ microwave dielectric ceramics for LTCC applications. *Mater Chem Phys* 2022, **289**: 126488.
[23] Zhou T, Liu YH, Song KX, *et al.* New low-ε_r, temperature stable $Mg_3B_2O_6$–$Ba_3(VO_4)_2$ microwave composite ceramic for 5G application. *J Am Ceram Soc* 2021, **104**: 3818–3822.
[24] Zhang ZW, Tang Y, Li J, *et al.* High-Q and near-zero τ_f composite $Li_2Mg_2TiO_5$–$Sr_3(VO_4)_2$ ceramics for low-temperature co-fired ceramic applications. *Ceram Int* 2020, **46**: 8281–8286.
[25] Zhou HT, Xu ZN, Yan JY, *et al.* Temperature-stable $BaAl_2Si_2O_8$–$CaSnSiO_5$ microwave dielectric ceramics. *Int J Appl Ceram Technol* 2022, **19**: 480–487.
[26] Lazoryak BI. Design of inorganic compounds with tetrahedral anions. *Russ Chem Rev* 1996, **65**: 287–305.
[27] Rosica N, Vladislav K. Crystal chemistry of "glaserite" type compounds. *Bulg Chem Commun* 2013, **45**: 418–426.
[28] Tsunooka T, Androu M, Higashida Y, *et al.* Effects of TiO_2 on sinterability and dielectric properties of high-Q forsterite ceramics. *J Eur Ceram Soc* 2003, **23**: 2573–2578.
[29] Song KX, Chen XM, Fan XC. Effects of Mg/Si ratio on microwave dielectric characteristics of forsterite ceramics. *J Am Ceram Soc* 2007, **90**: 1808–1811.
[30] Gao Y, Zheng Y, Lu XP, *et al.* Synthesis and microwave dielectric properties of $CaMg_2Si_3O_9$ ceramics. *J Mater Sci Mater Electron* 2020, **31**: 21583–21590.
[31] Huang FY, Su H, Zhang Q, *et al.* Effect of Sr^{2+} substitution on the Raman spectrum, phase composition and microwave dielectric properties of $CaMg_{1-x}Sr_xSi_2O_6$ ceramics. *Ceram Int* 2022, **48**: 3904–3911.
[32] Hameed I, Li L, Liu XQ, *et al.* Ultra low loss $(Mg_{1-x}Ca_x)_2SiO_4$ dielectric ceramics (x = 0 to 0.15) for millimeter wave applications. *J Am Ceram Soc* 2022, **105**: 2010–2019.
[33] Bafrooei HB, Liu B, Su WT, *et al.* $Ca_3MgSi_2O_8$: Novel low-permittivity microwave dielectric ceramics for 5G application. *Mater Lett* 2020, **263**: 127248.
[34] Zhang PC, Chen XQ, Chen GT, *et al.* Structural dependence of microwave dielectric properties of $Ca_3MgSi_2O_8$ ceramics. *J Mater Sci* 2022, **57**: 10039–10050.
[35] He YH, Wei XL, He GQ, *et al.* Sintering behavior, phase composition, microstructure, and dielectric properties of low-permittivity alkaline earth silicate $Sr_3MgSi_2O_8$ ceramics. *J Mater Sci Mater Electron* 2022, **33**: 26263–26275.
[36] Rodríguez-Carvajal J. Recent advances in magnetic structure determination by neutron powder diffraction. *Phys B Condens Matter* 1993, **192**: 55–69.
[37] Yang Z, Lu Y, Zhao Q, *et al.* X-ray diffraction rietveld refinement and its application in cathode materials for lithium-ion batteries. *J Inorg Mater* 2023, **38**: 589.
[38] Courtney WE. Analysis and evaluation of a method of measuring the complex permittivity and permeability microwave insulators. *IEEE Trans Microw Theory Tech* 1970, **18**: 476–485.
[39] Hakki BW, Coleman PD. A dielectric resonator method of measuring inductive capacities in the millimeter range. *IEEE Trans Microw Theory Tech* 1960, **8**: 402–410.
[40] Kresse G, Furthmüller J. Efficiency of *ab-initio* total energy calculations for metals and semiconductors using a plane-wave basis set. *Comput Mater Sci* 1996, **6**: 15–50.
[41] Baroni S, de Gironcoli S, dal Corso A, *et al.* Phonons and related crystal properties from density-functional perturbation theory. *Rev Mod Phys* 2001, **73**: 515–562.
[42] Kroumova E, Aroyo MI, Perez-Mato JM, *et al.* Bilbao crystallographic server: Useful databases and tools for phase-transition studies. *Phase Transitions* 2003, **76**: 155–170.
[43] Diao CL, Wang CH, Luo NN, *et al.* First-principle calculation and assignment for vibrational spectra of $Ba(Mg_{1/3}Nb_{2/3})O_3$ microwave dielectric ceramic. 2014, **115**: 114103.
[44] Klaver TPC, Madsen GKH, Drautz R. A DFT study of formation energies of Fe–Zn–Al intermetallics and solutes. *Intermetallics* 2012, **31**: 137–144.
[45] Kirklin S, Saal JE, Meredig B, *et al.* The open quantum materials database (OQMD): Assessing the accuracy of DFT formation energies. *npj Comput Mater* 2015, **1**: 15010.
[46] Park SG, Magyari-Köpe B, Nishi Y. Electronic correlation effects in reduced rutile TiO_2 within the LDA+U method. *Phys Rev B* 2010, **82**: 115109.
[47] Yonezaki Y. $(Ba,Sr)_3MgSi_2O_8$ structure change caused by Ba/Sr replacement. *Powder Diffr* 2015, **30**: 40–51.
[48] Park CH, Hong ST, Keszler DA. Superstructure of a phosphor material $Ba_3MgSi_2O_8$ determined by neutron diffraction data. *J Solid State Chem* 2009, **182**: 496–501.
[49] Yonezaki Y, Yanai R. X-ray induced electron defects in photochromic $Ba_3MgSi_2O_8$:Eu^{3+} and isostructural $K_3Na(SO_4)_2$. *J Alloys Compd* 2021, **876**: 160111.
[50] Yonezaki Y. Structural influence on photochromic behaviors of Eu^{2+}-doped glaserite-type silicates. *J Lumin* 2018, **195**: 408–412.
[51] Shannon RD. Revised effective ionic radii and systematic studies of interatomic distances in halides and chalcogenides. *Acta Crystallogr Sect A* 1976, **32**: 751–767.
[52] Iwata T, Horie T, Fukuda K. Reinvestigation of crystal structure and structural disorder of $Ba_3MgSi_2O_8$. *Powder Diffr* 2009, **24**: 180–184.
[53] Fukuda K, Ito M, Iwata T. Crystal structure and structural disorder of $(Ba_{0.65}Ca_{0.35})_2SiO_4$. *J Solid State Chem* 2007, **180**: 2305–2309.
[54] Ye H, Li Y, Sun JL. Kinetic study on the anisotropic grain growth of elongated iron-containing mullite. *Ceram Int* 2019, **45**: 12934–12941.
[55] Mouiya M, Tingaud D, Tamraoui Y, *et al.* Crystallography and anisotropy of crystals shape in dense aluminum titanate ceramics. *J Eur Ceram Soc* 2024, **44**: 4761–4771.
[56] Bosman AJ, Havinga EE. Temperature dependence of dielectric constants of cubic ionic compounds. *Phys Rev* 1963, **129**: 1593–1600.
[57] Wu FF, Zhou D, Du C, *et al.* A comprehensive study on crystal structure, phase compositions of the $BiVO_4$–$LaVO_4$ binary dielectric ceramic system and a typical design of dielectric resonator antenna for C-band applications. *Appl Mater Today* 2024, **38**: 102222.
[58] Shannon RD. Dielectric polarizabilities of ions in oxides and fluorides. *J Appl Phys* 1993, **73**: 348–366.

[59] Lyddane RH, Sachs RG, Teller E. On the polar vibrations of alkali halides. *Phys Rev* 1941, **59**: 673–676.
[60] Zhou D, Pang LX, Qi ZM. Crystal structure and microwave dielectric behaviors of ultra-low-temperature fired $x(Ag_{0.5}Bi_{0.5})MoO_4$–$(1–x)BiVO_4$ ($0.0 \le x \le 1.0$) solid solution with scheelite structure. *Inorg Chem* 2014, **53**: 9222–9227.
[61] Zhou D, Pang LX, Wang H, *et al.* Phase transition, Raman spectra, infrared spectra, band gap and microwave dielectric properties of low temperature firing $(Na_{0.5x}Bi_{1-0.5x})(Mo_xV_{1-x})O_4$ solid solution ceramics with scheelite structures. *J Mater Chem* 2011, **21**: 18412–18420.
[62] Pang LX, Zhou D, Yao XG, *et al.* Phase transitions and microwave dielectric behaviors of the $(Bi_{1-x}Li_{0.5x}Y_{0.5x})(V_{1-x}Mo_x)O_4$ ceramics. *J Am Ceram Soc* 2023, **106**: 3455–3461.
[63] Kim ES, Chun BS, Freer R, *et al.* Effects of packing fraction and bond valence on microwave dielectric properties of $A^{2+}B^{6+}O_4$ (A^{2+}: Ca, Pb, Ba; B^{6+}: Mo, W) ceramics. *J Eur Ceram Soc* 2010, **30**: 1731–1736.
[64] Wu FF, Zhou D, Du C, *et al.* Temperature stable $Sm(Nb_{1-x}V_x)O_4$ ($0.0 \le x \le 0.9$) microwave dielectric ceramics with ultra-low dielectric loss for dielectric resonator antenna applications. *J Mater Chem C* 2021, **9**: 9962–9971.
[65] Wang XY, Liu T, Cao ZK, *et al.* Lattice vibrational characteristics and structure-property relationships of $Ca(Mg_{1/2}W_{1/2})O_3$ microwave dielectric ceramics with different sintering temperatures. *Ceram Int* 2022, **48**: 1415–1422.
[66] Yin CZ, Zou ZY, Cheng MF, *et al.* Microwave dielectric properties of CaB_2O_4–$CaSiO_3$ system for LTCC applications. *Crystals* 2023, **13**: 790.
[67] Xue X, Li XM, Fu CL, *et al.* Sintering characteristics, phase transitions, and microwave dielectric properties of low-firing $[(Na_{0.5}Bi_{0.5})_xBi_{1-x}](W_xV_{1-x})O_4$ solid solution ceramics. *J Adv Ceram* 2023, **12**: 1178–1188.
[68] Li JM, Wang ZX, Guo YF, *et al.* Influences of substituting of $(Ni_{1/3}Nb_{2/3})^{4+}$ for Ti^{4+} on the phase compositions, microstructures, and dielectric properties of $Li_2Zn[Ti_{1-x}(Ni_{1/3}Nb_{2/3})_x]_3O_8$ ($0 \le x \le 0.3$) microwave ceramics. *J Adv Ceram* 2023, **12**: 760–777.
[69] Du K, Yin CZ, Guo YB, *et al.* Phase transition and permittivity stability against temperature of $CaSn_{1-x}Ti_xGeO_5$ ceramics. *J Eur Ceram Soc* 2022, **42**: 147–153.
[70] Su CX, Ao LY, Zhang ZW, *et al.* Crystal structure, Raman spectra and microwave dielectric properties of novel temperature-stable $LiYbSiO_4$ ceramics. *Ceram Int* 2020, **46**: 19996–20003.
[71] Cheng K, Tang Y, Xiang HC, *et al.* Two novel low permittivity microwave dielectric ceramics Li_2TiMO_5 (M = Ge, Si) with abnormally positive τ_f. *J Eur Ceram Soc* 2019, **39**: 2680–2684.
[72] Song XQ, Du K, Zou ZY, *et al.* Temperature-stable $BaAl_2Si_2O_8$–$Ba_5Si_8O_{21}$-based low-permittivity microwave dielectric ceramics for LTCC applications. *Ceram Int* 2017, **43**: 14453–14456.
[73] Manu KM, Karthik C, Leu LC, *et al.* Crystal structure and microwave dielectric properties of $LiRE_9(SiO_4)_6O_2$ ceramics (RE = La, Pr, Nd, Sm, Eu, Gd, and Er). *J Am Ceram Soc* 2013, **96**: 1504–1511.
[74] Kweon SH, Joung MR, Kim JS, *et al.* Low temperature sintering and microwave dielectric properties of B_2O_3-added $LiAlSiO_4$ ceramics. *J Am Ceram Soc* 2011, **94**: 1995–1998.
[75] Thomas S, Sebastian MT. Microwave dielectric properties of $SrRE_4Si_3O_{13}$ (RE=La, Pr, Nd, Sm, Eu, Gd, Tb, Dy, Er, Tm, Yb, and Y) ceramics. *J Am Ceram Soc* 2009, **92**: 2975–2981.
[76] Mao ZY, Chen JJ, Sun L, *et al.* Control of green emitting intermediate phases in $(Ba,Sr)_3MgSi_2O_8$:Eu^{2+},Mn^{2+} phosphors for dual-bands or tri-bands emission. *Mater Res Bull* 2015, **70**: 908–913.
[77] Song XQ, Xie MQ, Du K, *et al.* Synthesis, crystal structure and microwave dielectric properties of self-temperature stable $Ba_{1-x}Sr_xCuSi_2O_6$ ceramics for millimeter-wave communication. *J Materiomics* 2019, **5**: 606–617.
[78] Khan N, Dollimore D, Alexander K, *et al.* The origin of the exothermic peak in the thermal decomposition of basic magnesium carbonate. *Thermochim Acta* 2001, **367**: 321–333.
[79] Peng R, Lu YC, Zhang Q, *et al.* Amelioration of sintering and multi-frequency dielectric properties of $Mg_3B_2O_6$: A mechanism study of nickel substitution using DFT calculation. *J Adv Ceram* 2021, **10**: 1398–1407.